

## Experimental and theoretical investigation of large-amplitude oscillations of liquid droplets

By E. BECKER, W. J. HILLER AND T. A. KOWALEWSKI

Max-Planck-Institut für Strömungsforschung, Bunsenstrasse 10, 3400 Göttingen, Germany

(Received 21 June 1990)

Finite-amplitude, axially symmetric oscillations of small (0.2 mm) liquid droplets in a gaseous environment are studied, both experimentally and theoretically. When the amplitude of natural oscillations of the fundamental mode exceeds approximately 10% of the droplet radius, typical nonlinear effects like the dependence of the oscillation frequency on the amplitude, the asymmetry of the oscillation amplitude, and the interaction between modes are observed. As the amplitude decreases due to viscous damping, the oscillation frequency and the amplitude decay factor reach their asymptotical values predicted by linear theory. The initial behaviour of the droplet is described quite satisfactorily by a proposed nonlinear inviscid theoretical model.

### 1. Introduction

The problem of oscillating droplets has been an object of intense study for more than a century, both to gain a theoretical understanding (Kelvin 1890; Chandrasekhar 1959, 1961; Reid 1960; Prosperetti 1977, 1980*a, b*) and also in view of various technological applications (Valentine, Sather & Heideger 1965; Strani & Sabetta 1988). The first mathematical model of linear droplet oscillations in vacuum in the case of an inviscid fluid is due to Rayleigh (1879). The generalized linear solution of the problem which includes the influence of a surrounding medium is given by Lamb (1932). The solution describes the instantaneous deformation of the droplet shape by an infinite series of the surface spherical harmonics, where each term of this function corresponds to one independent natural oscillation mode. The axially symmetric form of this solution is

$$R(\theta, t) = R_0 \left\{ 1 + \sum_{l=0}^{\infty} a_l(t) P_l(\cos \theta) \right\}, \quad (1)$$

where  $P_l(\cos \theta)$  are the Legendre polynomials,  $R_0$  is the unperturbed radius of the droplet,  $a_l$  is the instantaneous amplitude of the  $l$ th mode of oscillation, and  $\theta$  is the polar angle of the spherical coordinate system with its origin at the centre of the spherical drop. The frequency  $\Omega_l$  of the  $l$ th oscillation mode of a liquid drop in vacuum or in air is given by

$$\Omega_l^2 = \frac{\sigma l(l-1)(l+2)}{\rho R_0^3}, \quad (2)$$

where  $\sigma$  is the surface tension of the droplet medium and  $\rho$  is its density. Subsequent linear analyses have included the viscosity of the droplet (Chandrasekhar 1959; Reid 1960) and, later, viscous effects of an outer fluid (Miller & Scriven 1968). The derived general dispersion equation describes small-amplitude oscillations of the viscous

droplet in the viscous medium. However for low-viscosity liquids (e.g. water, ethanol) and relatively large droplets ( $R_0 \geq 50 \mu\text{m}$ ) in dynamically inactive surroundings the general description simplifies and the so-called irrotational approximation, previously obtained by Lamb (1932), applies. Then, the decay time and the oscillation frequency are given by

$$\tau_l = \frac{\rho R_0^2}{\mu(l-1)(2l+1)} \quad (3)$$

and

$$\Omega_l^* = \Omega_l(1 - (\Omega_l \tau_l)^{-2})^{\frac{1}{2}}. \quad (4)$$

The viscosity,  $\mu$ , of the fluid reduces the natural oscillation frequency. This effect is of second order so that the frequency shift for low-viscosity liquids is negligibly small. Equation (3) shows that damping increases very quickly for higher oscillation modes. Therefore, in most cases the description of the droplet oscillation given by (1) is limited to the first few modes.

In their normal mode analysis of the initial motion of the viscous droplet in vacuum Chandrasekhar (1959), Prosperetti (1980*a, b*) and Brosa (1988) found that for each surface mode an infinite discrete frequency spectrum exists. This is apparently due to the viscosity, which is responsible for the vorticity generation by a free moving surface. Hence, the initial behaviour of a viscous droplet may apparently deviate from the least-damped normal modes (Prosperetti 1977) which are described by a damped harmonic oscillation. However, asymptotically with time only these modes remain. Prosperetti (1980*b*) shows that these viscous effects become negligibly small if the dimensionless viscosity  $\mu/(\rho\sigma R_0)^{\frac{1}{2}} < 0.1$ . This condition is fulfilled in the experiments presented here, therefore it is assumed that for small oscillation amplitudes the irrotational approximation given by (3) and (4) still applies.

Nonlinear oscillations of a droplet were analysed by Tsamopoulos & Brown (1983), but only for the case of inviscid liquids. Looking for strictly periodic oscillations they have found that the oscillation frequency of the fundamental mode decreases with increasing amplitude. The effect of small viscosity was incorporated into a nonlinear numerical study by Lundgren & Mansour (1988). They found that viscosity may have a relatively large effect on the behaviour of the higher oscillation modes, changing their near-harmonic resonance coupling with the fundamental mode  $l = 2$ .

Experimental measurements performed by Trinh, Marston & Robey (1987), Hiller & Kowalewski (1989*a*) for small oscillation amplitudes confirm the values of  $\Omega_2$  predicted by the linear theory for the fundamental mode. The only experimental work dealing with large-amplitude oscillations of droplets that we could find is that of Trinh & Wang (1982). Their experiment was performed on drops suspended in a neutrally buoyant and immiscible liquid. The results confirm qualitatively the predictions of the above nonlinear theories, i.e. the decrease of the oscillation frequency with increasing amplitude.

The lack of available experimental data concerning the nonlinear behaviour of droplets oscillating in air encouraged us to undertake the present investigation. The present study of nonlinear droplet dynamics is an inherent part of the method of measuring dynamic values of surface tension developed in Hiller & Kowalewski (1989*a*). Unfortunately, both of the above-mentioned theoretical analyses have very limited applicability to our experimental studies of the droplet oscillations. The first one (Tsamopoulos & Brown), with its accuracy limited to second-order effects, does not provide a method of checking the accuracy of the results obtained. The second

analysis (Lundgren & Mansour) seems to be rather difficult to be implemented practically for the measurements of dynamic surface tension as it is a pure numerical method and comparison of its results with our experimental data would require additional surface parameterization. Hence, in the following, we will describe the experimental method and results obtained for free oscillating droplets, followed by a new nonlinear model of inviscid droplet oscillations, which allows us to analyse the experimental data.

## 2. Experimental

### 2.1. The apparatus and method

The overall experimental arrangement is shown schematically in figure 1. The droplets were generated by the controlled breakup of a laminar jet discharging from a convergent nozzle into a gaseous environment. The pressure inside the plenum chamber of the nozzle is modulated by a piezoceramic transducer, described previously (Hiller & Kowalewski 1989*a*). The resulting jet perturbations are proportional to the voltage  $U V_{pp}$  applied to the transducer. By proper choice of the modulation, practically monodispersed droplets oscillating in axially symmetric modes are generated during the breakup process of the jet. The required droplet radius, within the range 100 to 300  $\mu\text{m}$ , is obtained by varying the jet radius which is about half that of the droplets. Once a droplet is detached from the liquid jet, it becomes an isolated mass of fluid suspended in space. Any subsequent motion of this isolated mass depends primarily on the surface tension forces and the velocity distribution in the fluid at the instant of breakoff from the jet. The initial velocity distribution and subsequent accelerations created by the surface tension force produce, owing to the viscosity, damped oscillatory motion of the droplet until it reaches its equilibrium spherical shape.

Initial deformations of the droplet observed after its detachment from the jet are illustrated in figure 2. As the droplet velocity is relatively small (a few m/s) the influence of aerodynamic forces on its shape is assumed to be negligibly small. The droplet is observed through a microscope in bright field illumination. A pulsed light-emitting-diode (LED) is used as a light source (Stasicki, Hiller & Meier 1990). The exposure times are below 0.2  $\mu\text{s}$ . The images of the droplet are registered by CCD camera (Sony XC77CE). Data acquisition and storage are performed with a 386 Personal Computer (IBM compatible) equipped with an 8-bit digitizing board VS100/768 (Imaging Technology Inc.) and 140 Mbyte hard disk. All further processing of the images (image analysis and shape fitting) takes place on  $\mu\text{VAX II}$  and IBM3090 computers respectively.

Two methods of imaging are applied. First is a multi-exposure method, shown in figure 2. This method, described in detail previously (Hiller & Kowalewski 1989*b*), provides high temporal and spatial resolution for about one oscillation period. However, to extend the observation time, a rather tedious matching procedure to combine phases of separate observations done at different distances from the nozzle is required. Therefore, to facilitate observation of the droplets during longer periods a second recording method, based on a beat-frequency stroboscopic technique, was developed. For this purpose a digital phase-scanning device (Hiller, Kowalewski & Stasicki 1989) is used to change continuously the phase of the pulses triggering the LED drive, relative to the phase of the jet modulating frequency. Thus the stroboscopically observed phenomena slowly change their phase and their development in time can be easily recorded. By changing synchronously the position

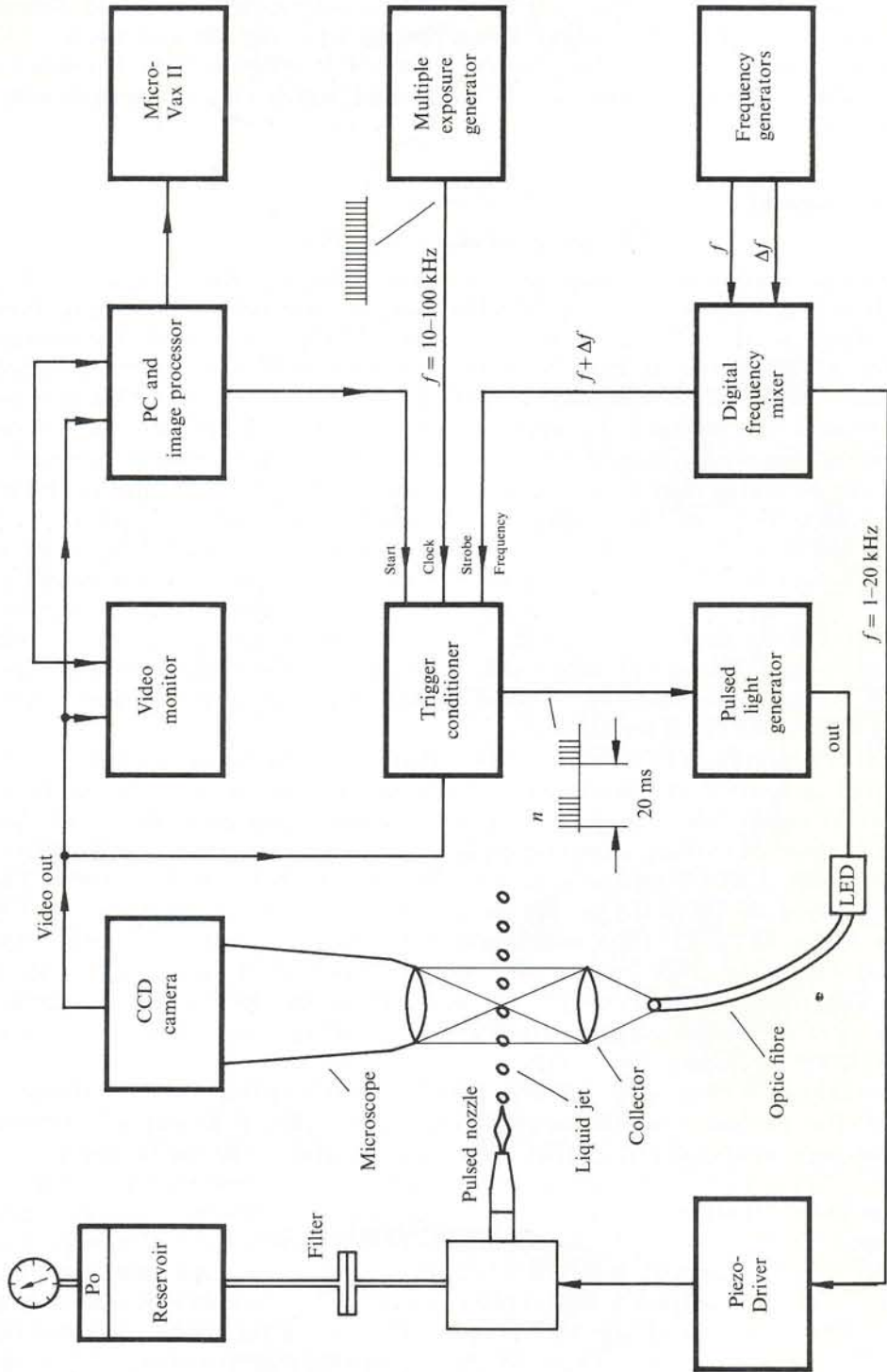


FIGURE 1. Experimental set-up.

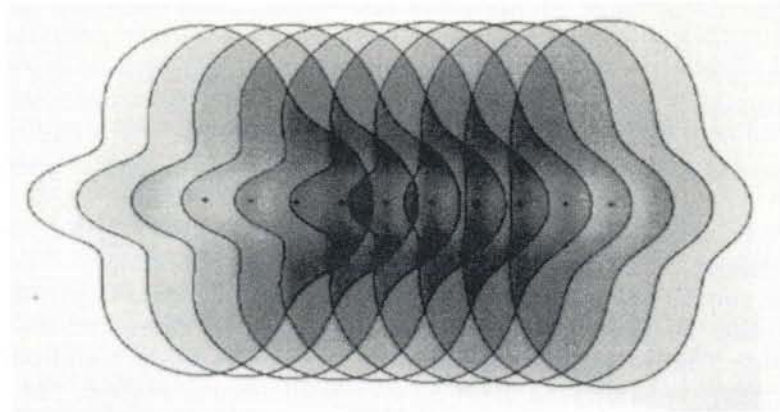


FIGURE 2. Multiexposure of an oscillating droplet observed a short time after its generation. The equilibrium radius of the droplet  $R_0 = 210 \mu\text{m}$ , the time interval between exposures is  $7.8 \mu\text{s}$ . The solid line is function (5) with  $l_{\text{max}} = 10$  fitted to the droplet boundaries.

of the camera, the development of the droplet shape is followed along its trajectory from the point of separation till it reaches the spherical form. This is possible as the reproducibility of the droplets generated by the controlled jet breakup is extremely high. Using this technique, the images of the droplet were recorded periodically by an image processor and stored on a hard disk of the computer. Usually sequences of 200–300 images are taken. The recording time of one image is 3.6 s (time needed to save one image on the disk). The 'real time' resolution, controlled by the beat frequency, is kept in the range of 10–30  $\mu\text{s}$ . It allows the registration of several periods of droplet oscillations in one sequence of images.

### 2.2. Analysis of the droplet images

As we can observe only the projection of a droplet, we must assume that its shape is convex and axially symmetric with respect to the nozzle axis, and that the axis of symmetry is parallel to the plane of observation (i.e. the sensor area of the camera). The three-dimensional form of a droplet is then completely defined by its contour  $R(\theta, t)$ . We assume also that a limited number of modes ( $l_{\text{max}}$ ) suffices to describe the deformation of the droplet and that its volume remains constant (incompressible fluid). To fulfil the last condition we have to modify (1), replacing unity by a volume correction term  $\delta(t)$ . This term is a function of time  $t$  only. The momentary description of the droplet surface by Legendre polynomials remains unaffected and is given by

$$R(\theta, t) = R_0 \left\{ \delta(t) + \sum_{l=2}^{l_{\text{max}}} a_l(t) P_l(\cos \theta) \right\}. \quad (5)$$

The first expansion term is  $l = 2$  as  $l = 0$  and  $l = 1$  describe respectively the volumetric pulsation and the translatory motion of the droplet. The value of  $\delta(t)$  is calculated from the following equation:

$$\frac{4}{3}\pi R_0^3 - 2\pi \int_0^\pi \frac{R^3(\theta, t)}{3} \sin \theta \, d\theta = 0. \quad (6)$$

The value of  $\delta$ , in practice, is very close to unity and therefore introduces only a slight modification into (1). However, this correction is needed for a precise determination of the volume of the droplets, which is not known *a priori* in the experiments. For

the practical evaluation of the coefficients of (5) the images of the droplet taken at corresponding moments of exposure are first traced using computer-aided image analysis to draw out points of droplet boundaries. Up to 900 points are usually identified during this procedure. To speed up further calculation the number of points is reduced. First, smoothing the data with a FFT low-pass filter the stray points are eliminated. Then, about 100 'representative', uniformly distributed points are selected. These points are used to match the shape given by the function (5).

The analysis of the oscillations is in most cases limited to  $l_{\max} = 5$ . As the first mode of interest is  $l = 2$ , the fit depends on eight parameters: four surface deformation amplitudes ( $a_2$ – $a_5$ ), the unknown equilibrium radius  $R_0$  of a droplet, two coordinates and the rotation angle of a coordinate system connected with an image of the droplet. The least-square fitting of (5) to the previously found points of the droplet boundary is based on a quasi-Newton optimization method. The vectorized computer code run on an IBM 3090-300E allows fitting of one droplet image with typically 100 points in about 0.5 s of CPU time. For some cases, especially at higher deformation amplitudes, the number of analysed modes was increased to  $l_{\max} = 10$ , extending calculation time to about 2 s.

In order to compare the experimental results for droplet oscillations with theoretical predictions quantitatively, the correct value of the droplet radius  $R_0$  must be known. The accuracy of measured droplet coordinates is directly proportional to the resolution of the optical system, which amounts to one pixel in the image plane. In our experiments the droplet images have mean diameters of about 250 pixels (the format of the sensor being  $756 \times 581$  square pixels). Owing to the short exposure time (200 ns) the blur due to the droplet motion is smaller than one pixel and can be neglected. Thus a single point of the image is defined with an accuracy better than 0.5%. The mean fitting error is typically 0.3 pixels for oscillation amplitudes up to  $a_2 = 0.5$ . Hence, we may estimate the error of the measured droplet radius to be smaller than 0.2%.

The other source of possible errors is the presence of non-axially symmetric modes of oscillation. These will appear as fluctuations of the droplet radius  $R_0$  obtained from the fitting procedure and such data are not the subject of further analysis. Owing to the high spatial resolution of the imaging system even small changes of the droplet radius due to its evaporation can be observed and measured. In the present experiment with ethanol droplets of about 200  $\mu\text{m}$  radius moving in the air, the measured rate of radius contraction was below  $2 \times 10^{-4}$  m/s. It corresponds to approximately a 1.5% variation of the oscillation frequency  $\Omega_l$  during 10 ms observation time. This effect was taken into account when analysing the observed oscillations of the droplets (see Appendix A). The instant of image exposure is determined with an accuracy of 0.1% of the oscillation period of the droplet.

### 2.3. Experimental results

The experiments were performed with ethanol (95%) (denatured with methyl-ethyl-ketone) as a droplet medium. The physical properties of the liquid used measured by standard methods at 295 K are: density  $\rho = 803 \pm 1$  kg/m<sup>3</sup>, viscosity  $\mu = 1.2 \pm 0.1$  mPa s and surface tension  $\sigma = 22.9 \pm 0.3$  mN/m. The droplets are dispersed in air at normal atmospheric pressure and room temperature  $295 \pm 1$  K.

The droplets generated during breakup of the jet are usually interspersed with smaller satellite droplets. Depending on the nature of the applied initial jet disturbance a satellite droplet will merge with the following or the leading droplet at

some distance from the nozzle. This changes the droplet mass and generates an additional perturbation of its surface. Chaudhary & Maxworthy (1980) have demonstrated that varying the jet perturbation frequency and amplitude, and adding the third harmonic to the fundamental enables one to control the behaviour of the satellite drops and in some cases effects their elimination. The complete elimination of satellites requires large amplitudes of the jet perturbation which initiate strongly nonlinear oscillations of the generated droplets.

In the following we present results obtained for an oscillating droplet generated at relatively small perturbation amplitude in the presence of a satellite droplet, and a droplet created without a satellite using large perturbation amplitudes with the fundamental frequency accompanied by its third harmonic.

Figures 3(a)–3(d) display a short ( $\approx 4$  ms) time sequence of the instantaneous dimensionless oscillation amplitudes  $a_l$  of a droplet for the modes  $l = 2, 3, 4$  and  $5$  respectively. The values of  $R_0$  and  $a_l$  are obtained from a series of 179 images of the droplet with the help of the fitting procedure described in §2.2. The mean undisturbed radius  $\bar{R}_0$  of the droplet, calculated as an arithmetic mean of the values  $R_0$ , is equal to  $177 \mu\text{m}$ . The droplet is generated at a relatively small perturbation amplitude of the jet. The input voltage of the jet modulator  $U$  is equal  $1 \text{ V}_{\text{pp}}$ . The registration of the droplet oscillations begins shortly after it merges with a satellite droplet. The initial amplitude of the second mode (figure 3a) is about 0.3, whereas the amplitude of the third mode (figure 3b) is about 3 times smaller. In accordance with (3) the viscous damping becomes stronger with increasing mode number, as can be also seen from figure 3(c, d), where the higher modes  $l = 4, 5$  are displayed.

At first glance, the waveform of the oscillations for  $l = 2, 3$  seems to be that of a damped harmonic oscillator. A more careful analysis, however, reveals small variations of the oscillation period and an asymmetry between the positive (prolate) and negative (oblate) displacements. This type of oscillation may be simulated by introducing into the equation of motion of a damped harmonic oscillator a restoring force with a symmetric term (i.e. depending on even powers of the displacement). Using an asymptotic expansion for small amplitudes, we obtain the following time-dependent approximation for  $a_l$ :

$$a_l(t) = A_l \sin \{N\Omega_l [(1 - (\Omega_l \tau_l)^{-2})^{\frac{1}{2}} + \alpha_l A_l^2] t + \phi_l\} + \beta_l A_l^2. \quad (7)$$

The amplitude damping is given by

$$A_l(t) = A_{0l} \exp(-t/\tau_l). \quad (8)$$

Here, the term with  $\alpha_l$  accounts for the amplitude dependence of the oscillation frequency,  $\beta_l$  represents the asymmetry of the amplitude  $a_l(t)$ , and  $\phi_l$  is the phase angle. A slight decrease of the droplet radius due to evaporation, observed during longer time sequences, is compensated with help of the normalization function  $N(t)$  defined in Appendix A (A 1).

The six free parameters:  $\alpha_l$ ,  $\beta_l$ ,  $\tau_l$ ,  $\Omega_l$ ,  $\gamma_l$ , and  $A_{0l}$  were used to fit (7) and (8) to the measured values of the instantaneous amplitudes  $a_2$  and  $a_3$ . The fitting procedure is based on the quasi-Newton optimization method mentioned earlier. The 'best fit' curves displayed in figure 3(a, b) were obtained for the following values of the fitting parameters:  $\Omega_2 = 5939 (6414) \text{ s}^{-1}$ ,  $\tau_2 = 3.953 (4.193) \times 10^{-3} \text{ s}$ ,  $\alpha_2 = -0.19$ ,  $\beta_2 = 0.21$ ,  $\Omega_3 = 11342 (12421) \text{ s}^{-1}$ ,  $\tau_3 = 1.552 (1.497) \times 10^{-3} \text{ s}$ ,  $\alpha_3 = -29.5$ ,  $\beta_3 = 3.59$ . For comparison the corresponding values of the linear theory, calculated from (2) and (3) by inserting measured values of  $\sigma$  and  $\mu$ , are written in brackets.

The observed weak increase of the oscillation frequency is well described by the parameter  $\alpha_2$ . However, owing to the short registration time and still large final

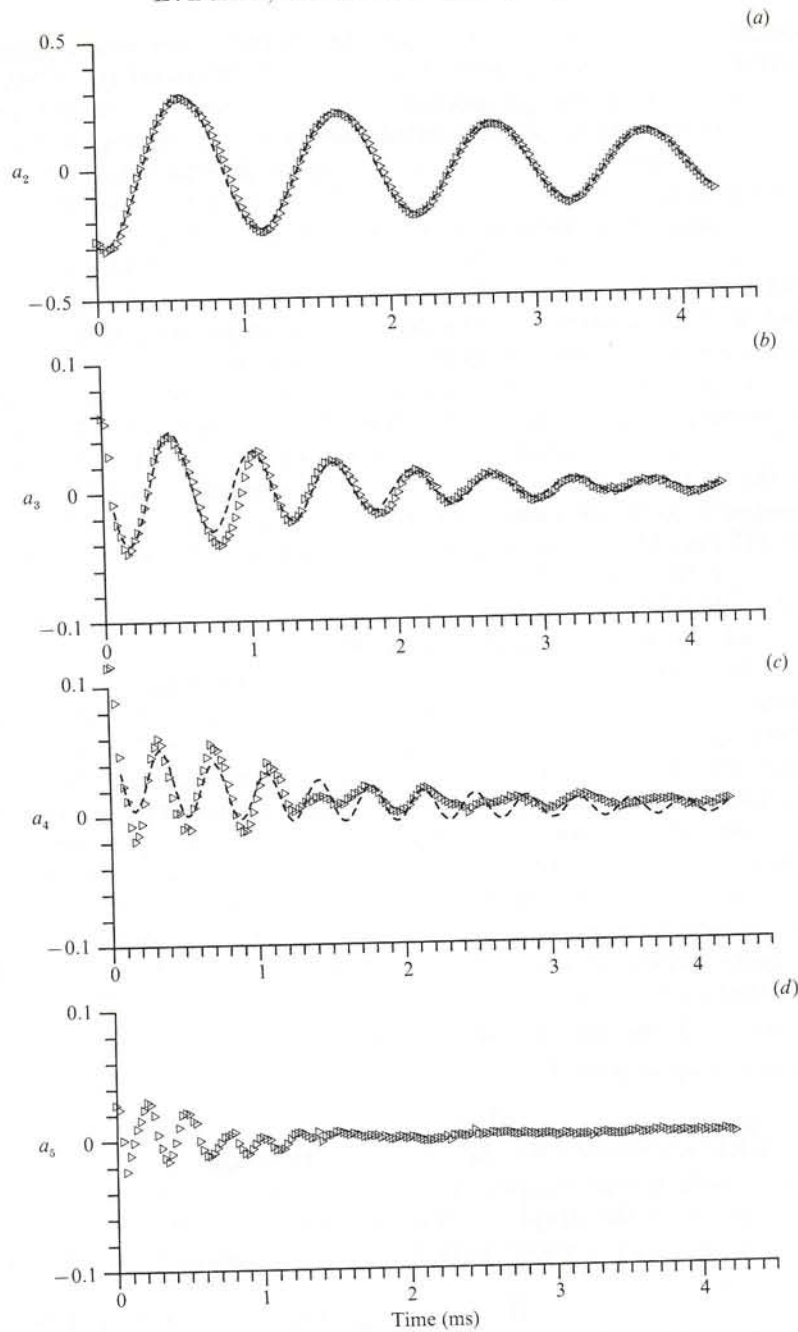


FIGURE 3. Measured oscillation amplitudes of an ethanol droplet. Jet excitation with  $1 V_{pp}$ . (a) Mode  $l=2$ ; (b)  $l=3$ ; (c)  $l=4$ ; (d)  $l=5$ . Dashed line - best fit of the functions (7) and (8).

amplitudes of the oscillations ( $A_2(t=3 \text{ ms}) > 0.1$ ) the fitting procedure does not give the correct asymptotic behaviour of the analysed curve. This brings out discrepancies between asymptotic and expected values of the oscillation frequency. Higher oscillation modes ( $l=4, 5$ ) demonstrate strong nonlinearities and the asymptotic analysis given by (7) and (8) fails for these modes.

Oscillation amplitudes for a number of consecutive periods, from the droplet

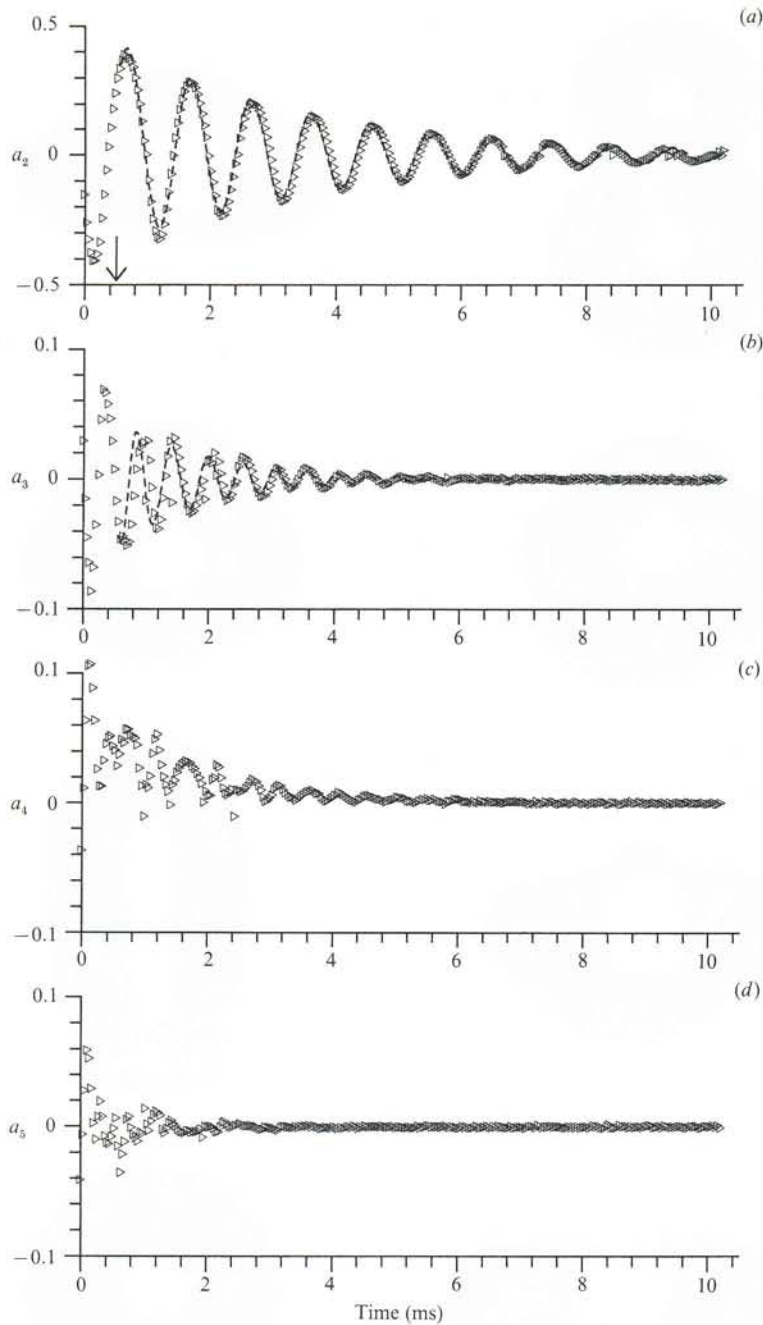


FIGURE 4(a-d). As figure 3 but jet excitation with  $3 V_{pp}$ . The arrow indicates the moment when the droplet merges with the satellite droplet.

generation nearly at the jet tip until their disappearance, including the absorption of the satellite droplet, are displayed in figure 4. The mean droplet radius is  $172 \mu\text{m}$  and the perturbation amplitude of the jet is still small ( $U = 3 V_{pp}$ ). The fitting procedure here gives quite reasonable approximations of the damping factor and of the asymptotic value of the oscillation frequency. The 'best fit' parameters (beginning after the satellite merging) and the corresponding 'linear theory values'

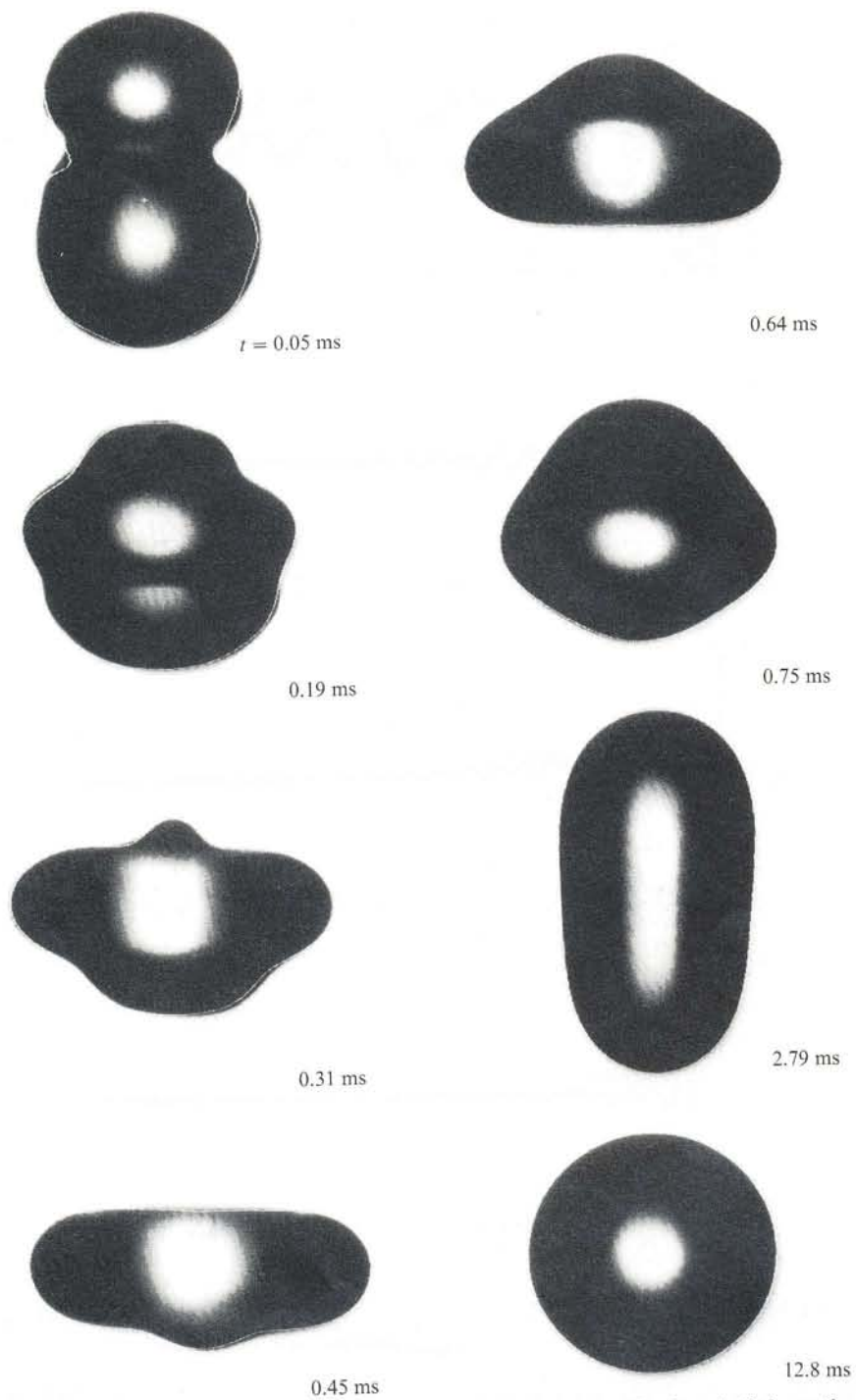


FIGURE 5. Images of oscillating droplets at different moments after the breakoff from the jet. The solid line is function (5) with  $I_{\max} = 10$  fitted to the droplet boundaries.

are  $\Omega_2 = 6440$  (6696)  $s^{-1}$ ,  $\tau_2 = 3.448$  (3.959)  $\times 10^{-3}$  s,  $\alpha_2 = -0.88$ ,  $\beta_2 = 0.36$ ,  $\Omega_3 = 13420$  (12966)  $s^{-1}$ ,  $\tau_3 = 1.474$  (1.414)  $\times 10^{-3}$  s,  $\alpha_3 = 333$ ,  $\beta_3 = -1.8$ .

It is interesting to note that the enhancement of nonlinear effects, expected due to the larger initial amplitude of oscillations, is evident mostly at the higher oscillation modes (figure 4*c, d*). The nonlinear behaviour of the higher modes persists even when their amplitudes become very small. This effect, which is due to second- and third-order resonance coupling, was found by Brown and co-workers in their theoretical analysis (Tsamopoulos & Brown 1983; Natarajan & Brown 1987). The fundamental mode seems to be less affected, as even merging of the satellite, which results in a 1% increase of the droplet radius, has no visible influence on the evolution of its oscillations.

A more extreme example of droplet oscillation is displayed in figure 5. The jet is modulated with amplitudes of  $U = 150 V_{pp}$  at the fundamental frequency and  $50 V_{pp}$  at the third harmonic. The record of the droplet begins shortly after it breaks off from the jet. No satellite droplets are observed. The initial amplitude of the second mode reaches a value of  $A_{02} = 0.65$ . The mean undisturbed radius of the droplet is 202  $\mu\text{m}$ . To improve the fitting analysis given in §2.2, nine surface modes ( $l_{\text{max}} = 10$ ) are used. The mean fitting error for the first twenty images of the strongly deformed droplet is about 2.5% but for the following images reduces to 0.2%.

Figure 6 shows the measured amplitudes of the observed droplet oscillations. The nonlinear effects are evident for all analysed modes. The fundamental mode still has clearly regular oscillations but its frequency does not change monotonically in time: it increases initially and then decreases. Thus the asymptotic behaviour of this mode could be analysed with the help of equations (7) and (8) only for times greater than 2.5 ms. The values of the final oscillation frequency and damping factor so obtained are:  $\Omega_2 = 5275$  (5261)  $s^{-1}$ ,  $\tau_2 = 5.177$  (5.460)  $\times 10^{-3}$  s. The values are quite close to those given in brackets and obtained from (2) and (3). The initial oscillation frequency of the fundamental mode, found with (7) and (8) for the first 2.5 ms of the registration time, equals 3346  $s^{-1}$ . The corresponding frequency drift is  $\alpha_2 = -0.87$ . The droplet oscillations at higher modes exhibit nonlinearities which cannot be analysed with our simple approximation given by equations (7) and (8).

The following conclusions can be drawn from our experimental investigation:

(i) For small and moderate amplitudes of the fundamental mode the asymptotic behaviour of the droplet oscillations can be well described with help of the simple model given in (7) and (8). The resulting values of the initial oscillation frequency and damping factor correspond to those provided by the linear theory, justifying its applicability for low viscosity liquids. To some extent, the approximation used holds for the third mode. The quality of the fit, however, is no longer as good as for  $l = 2$ . For higher modes this description becomes unsatisfactory due to the pronounced mode interaction.

(ii) The nonlinearity of the fundamental mode appears mainly in the form of a frequency drift. Assuming a square dependence of the frequency on the amplitude, this decrease is described by the nonlinearity parameter  $\alpha_2$ . The value of  $\alpha_2$  found in our experiments is in the range of  $-0.6$  to  $-0.9$ . For an initial amplitude  $A_{02} = 0.65$ , which is about the highest value we observe in our experiments, the frequency of the second mode deviates from that calculated according to equation (2) by about 35%. This deviation decreases down to 5% for  $A_2 = 0.1$ .

(iii) In most of the cases observed up to now, the oscillation frequency monotonically increases as the amplitudes becomes small. However, for some breakup configurations, as in the last example shown, frequency modulation

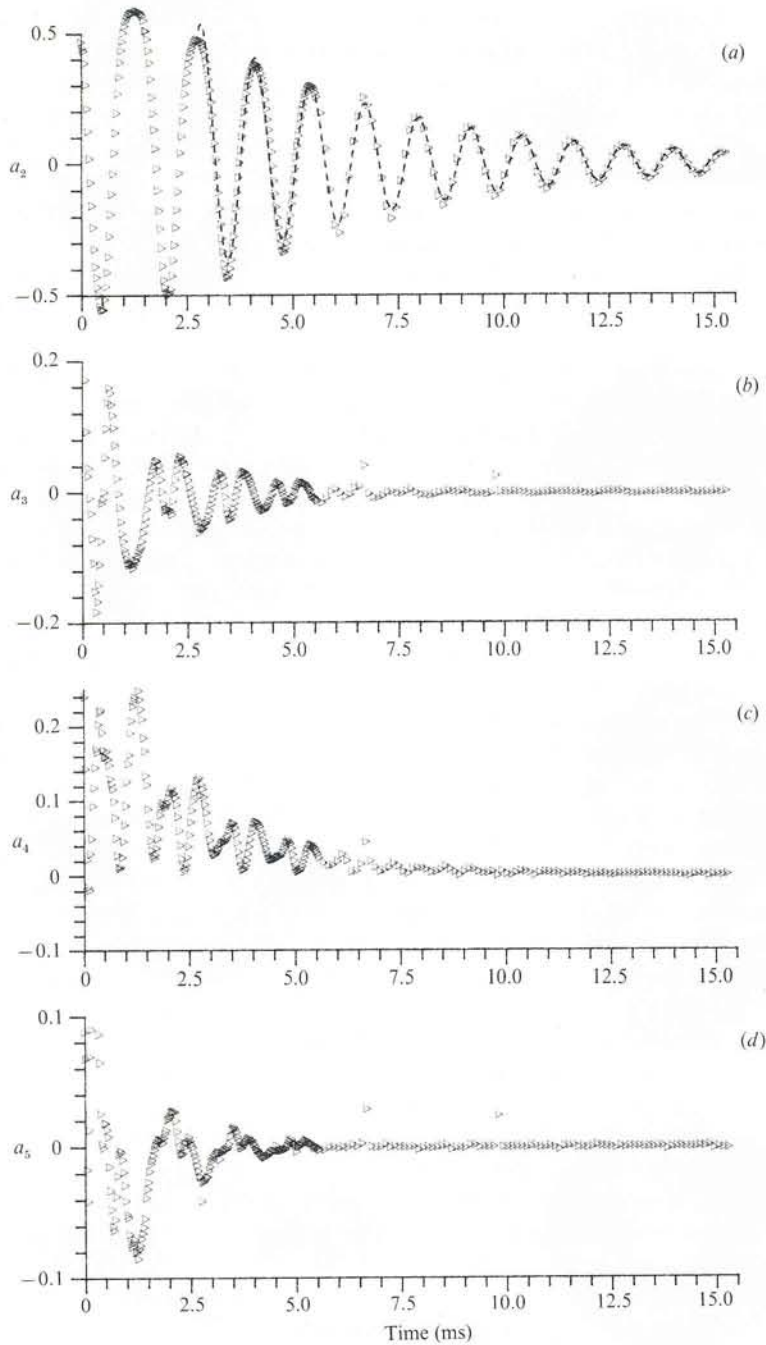


FIGURE 6. Measured oscillation amplitudes of the droplet shown in figure 5: large-amplitude excitation without satellite drops. (a) Mode  $l=2$ ; (b)  $l=3$ ; (c)  $l=4$ ; (d)  $l=5$ . Dashed line – best fit of the function (7) and (8) for time  $t > 2.5$  ms.

appears. In such cases the asymptotic analysis generally fails and can be applied only to the final behaviour of the oscillations.

(iv) The decay rate of the amplitude of the fundamental mode,  $\tau_2$ , is in most cases quite well described by the exponential relation (8).

(v) At relatively small amplitudes of the fundamental mode there seems to be a very weak excitation of modes  $l = 3$  and  $l = 4$  from the base mode  $l = 2$  (compare figures 3*b* and *c*). This is inferred from the observation that the decay rates  $\tau_2$  as well as  $\tau_3$  and  $\tau_4$ , measured in the above way, yield values very close to those calculated from equation (3). At larger fundamental-mode amplitudes (figures 4 and 6), a weak nonlinearity of this mode is accompanied by a strong nonlinear excitation of the higher modes. In this case their oscillation frequencies and damping factors cannot be described by the linear theory.

This 'oversensitiveness' of the higher oscillation modes, caused by nonlinear mode coupling, is obvious if we notice that most of the oscillation energy is stored in the fundamental mode. Therefore even a small energy transfer between the fundamental and a higher mode changes appreciably the energy balance of the last one.

Summarizing, the asymptotic approximation equations (7) and (8) cannot be applied for the determination of the variation of the frequency of the first few consecutive oscillations after the break-off of the droplet. However, they describe well the asymptotic variation of the frequency of the fundamental mode for a long enough series of droplet oscillations. As we mentioned earlier, there exists a practical demand for a precise determination of the instantaneous values of surface tension using large-amplitude droplet oscillations, and therefore it was necessary to develop a theoretical model taking in account all the nonlinear effects. As a first attempt, the full theory of the nonlinear inviscid droplet oscillations will be described and its features compared with our experimental findings.

### 3. Nonlinear model for inviscid droplet oscillations

Although the theoretical analysis of droplet oscillations for inviscid and irrotational fluid motion is generally of limited applicability for the study of real liquids, the usefulness of the inviscid linear model for the asymptotic description of the oscillations of low-viscosity droplets justifies our attempt to use an inviscid approximation for the nonlinear modelling. The numerical method we use is a least-squares approximation to the kinematic and normal stress boundary conditions. The simple parameterization of the droplet surface (equation (5)) allows us a straightforward comparison of numerical results with the experimental data.

#### 3.1. Mathematical formulation

We analyse the motion of a droplet of an inviscid and incompressible liquid in vacuum, or in a gas of negligible density. For simplicity our analysis is limited to the axially symmetric case. The movement of the surface has been given by equation (5). The assumption of constant droplet volume is satisfied by the volume correction function  $\delta(t)$ , given previously in equation (6). In the following calculations the maximum number of surface modes  $l_{\max}$  is set to 6, found to guarantee sufficient accuracy at a still reasonable computation time (see Appendix B).

The incompressible, irrotational and axially symmetric motion of the liquid in spherical polar coordinates  $(r, \theta)$  is described by the Laplace equation:

$$\nabla^2 \Phi(r, \theta, t) = 0, \quad 0 \leq r \leq R(\theta, t), \quad 0 \leq \theta \leq \pi, \quad (9)$$

with the velocity field given by

$$\mathbf{u}(r, \theta, t) = -\nabla \Phi(r, \theta, t). \quad (10)$$

Expanding the potential  $\Phi$  in partial solutions of the Laplace equation with

expression coefficients linear in the time derivatives  $\dot{a}_l(t)$  of the surface amplitudes, we can write

$$\Phi(r, \theta, t) = \sum_{l=2}^{l_{\max}} \Phi_l(r, \theta, t) \dot{a}_l(t) = \sum_{l=2}^{l_{\max}} \sum_{i=1}^{i_{\max}} c_{li}(t) \phi_i(r, \theta) \dot{a}_l(t), \quad (11)$$

where  $\phi_i(r, \theta) = r^i P_i(\cos \theta)$  and  $P_i(\cos \theta)$  are Legendre polynomials in  $\cos \theta$ .

From the kinematic boundary condition at the moving surface it follows that

$$\mathbf{u}(r = R(\theta, t), \theta, t) \cdot \mathbf{e}_n(\theta, t) = \frac{\partial R(\theta, t)}{\partial t} \mathbf{e}_r \cdot \mathbf{e}_n(\theta, t), \quad (12)$$

where,  $\mathbf{e}_n$ , the vector normal to the surface, is given by the unit vectors  $\mathbf{e}_r$  and  $\mathbf{e}_\theta$  of the coordinate system in the following form:

$$\mathbf{e}_n = \frac{R\mathbf{e}_r - (\partial_\theta R)\mathbf{e}_\theta}{[R^2 + (\partial_\theta R)^2]^{\frac{1}{2}}}. \quad (13)$$

The pressure difference across the surface must be balanced by the surface tension. Assuming for simplicity zero pressure outside the droplet, the pressure at the droplet surface is given by

$$p(r = R(\theta, t), \theta, t) = -2\sigma H(\theta, t), \quad (14)$$

where  $H$ , the mean curvature of the surface, is

$$H = -\frac{1}{2} \left( \frac{R^2 + 2(\partial_\theta R)^2 - R\partial_\theta^2 R}{((\partial_\theta R)^2 + R^2)^{\frac{3}{2}}} + \frac{R - \cot \theta \partial_\theta R}{R((\partial_\theta R)^2 + R^2)^{\frac{1}{2}}} \right). \quad (15)$$

The origin of our coordinate system is arbitrarily chosen and does not need to coincide with the centre of mass of the droplet. Moreover, it can be shown that during oscillations the centre of mass moves forward and backward in our coordinate system. Owing to the axial symmetry of the problem this movement takes place along the symmetry axis  $\theta = 0$ . The location of the mass centre at any time  $t$  can be found to be

$$\mathbf{e}_z s(a_2, \dots, a_{l_{\max}}) = \mathbf{e}_z \frac{3}{8} R_0 \int_{-1}^1 d(\cos \theta) \cos \theta \left( \delta(a_2, \dots, a_{l_{\max}}) + \sum_{l=2}^{l_{\max}} a_l P_l(\cos \theta) \right)^4; \quad (16)$$

$\mathbf{e}_z$  is the unit vector in the direction  $\theta = 0$ .

Therefore the acceleration of the coordinate system relative to the centre of mass is:

$$-\mathbf{e}_z \ddot{s} = -\mathbf{e}_z \sum_{l=2}^{l_{\max}} \left( \frac{\partial s}{\partial a_l} \ddot{a}_l + \sum_{m=2}^{l_{\max}} \frac{\partial^2 s}{\partial a_l \partial a_m} \dot{a}_m \dot{a}_l \right). \quad (17)$$

Hence, the Euler equation in our non-inertial coordinate system has the following form:

$$\partial_t \mathbf{u} + (\mathbf{u} \nabla) \cdot \mathbf{u} - \ddot{s} \mathbf{e}_z = -\frac{\nabla p}{\rho}. \quad (18)$$

By use of the Bernoulli integral and (10) we find the equation for the pressure inside the droplet:

$$p(r, \theta, t) = \rho(\partial_t \Phi(r, \theta, t) - \frac{1}{2}(\nabla \Phi(r, \theta, t))^2 + \ddot{s}(t)r \cos \theta + g(t)), \quad (19)$$

where  $g(t)$  is a time-dependent integration constant.

Combining (5) and (11) the kinematic boundary condition (12) takes the form

$$\sum_{i=1}^{i_{\max}} c_{li} \frac{\partial \phi_i(r = R, \theta, t)}{\partial n} (R^2 + (\partial_\theta R)^2)^{\frac{1}{2}} + R \frac{\partial R}{\partial a_l} = 0, \quad l = 2, \dots, l_{\max} \quad (20)$$

giving a set of equations for the expansion coefficients  $c_{li}$ .

As can be seen, the kinematic boundary condition should be now fulfilled not on the equilibrium spherical droplet (as in the case of the linear theory) but on the deformed droplet surface  $R(\theta, t)$ . This however is not automatically guaranteed by the assumed truncated expansion for the velocity potential (11). Therefore, instead of looking for the exact solution of (20), we try to find 'the best fitting' combination of the coefficients  $c_{li}$  by minimizing the following integrals:

$$\chi_l^2(\{c_{li}\}) = \int_{-1}^1 d(\cos \theta) L_l^2(\theta, \{c_{li}\}) \rightarrow \min, \quad l = 2, \dots, l_{\max}, \quad (21)$$

where,  $L_l(\theta, \{c_{li}\})$  is given by the left-hand side of the equation (20).

The minimization conditions (21) represent a system of linear algebraic equations ( $\partial \chi_l^2 / \partial c_{li} = 0$ ), from which the coefficients  $c_{li}$  can be found as functions of the droplet shape parameters  $a_l$  only:

$$c_{li}(t) = c_{li}(a_2(t), \dots, a_{l_{\max}}(t)). \quad (22)$$

The value  $l_{\max}$  - the limiting number of expansion terms in (20) - is chosen so that all relative errors of minimization

$$(\chi_{\text{rel}})_l^2 := \chi_l^2 / \int_{-1}^1 d(\cos \theta) \left[ R \frac{\partial R}{\partial a_l} \right]^2 \quad (23)$$

are below  $10^{-2}$ . For moderate deformation amplitudes ( $a_2 < 0.4$ ) this condition is fulfilled if  $l_{\max} = 12$ .

In an analogous way the second boundary condition (15) is solved to obtain the unknown function  $g(t)$  and the accelerations  $\ddot{a}_l(t)$  of the surface parameters. Substitution of the pressure in (14) by its representation given in (19) and expanding the velocity potential according to (11) results into the following equation:

$$\sum_{l=2}^{l_{\max}} \left( \Phi_l + \frac{\partial s}{\partial a_l} r \cos \theta \right) \ddot{a}_l + g + \frac{2\sigma}{\rho} H + \sum_{l,m=2}^{l_{\max}} \left( \frac{\partial \Phi_l}{\partial a_m} + \frac{\partial^2 s}{\partial a_l \partial a_m} r \cos \theta - \frac{1}{2} \nabla \Phi_l \nabla \Phi_m \right) \dot{a}_l \dot{a}_m = 0, \quad r = R(\theta, t), \quad (24)$$

which we solve by minimizing the integral over the square of its left-hand side  $\mathcal{L}^2(\theta, \{\ddot{a}_l\}, g)$

$$\mathcal{H}^2(\{\ddot{a}_l\}, g) = \int_{-1}^1 d(\cos \theta) \mathcal{L}^2(\theta, \{\ddot{a}_l\}, g) \rightarrow \min. \quad (25)$$

From (25) follows a system of  $l_{\max}$  linear algebraic equation for  $g(t)$  and  $\ddot{a}_l(t)$  ( $\partial \mathcal{H}^2 / \partial \ddot{a}_l = 0$ ;  $\partial \mathcal{H}^2 / \partial g = 0$ ).

The related relative error of minimization

$$\mathcal{H}_{\text{rel}}^2 = \mathcal{H}^2 / \int_{-1}^1 d(\cos \theta) \left( \sum_{l,m=2}^{l_{\max}} \left( \frac{\partial \Phi_l}{\partial a_m} + \frac{\partial^2 s}{\partial a_l \partial a_m} r \cos \theta - \frac{1}{2} \nabla \Phi_l \nabla \Phi_m \right) \dot{a}_l \dot{a}_m + \frac{2\sigma}{\rho} H \right)^2 \quad (26)$$

remains with the chosen limit  $l_{\max} = 6$  below  $10^{-2}$ .

Finally the surface motion of the droplet is given by a set of five nonlinear differential equations:

$$\ddot{a}_l = F_l(a_2, \dots, a_6, \dot{a}_2, \dots, \dot{a}_6). \quad (27)$$

It can be shown that the linearization of (20) and (24) leads to Lamb's linear equation:

$$\ddot{a}_l(t) = -\frac{\sigma l(l-1)(l+2)}{\rho R_0^3} a_l(t) \quad (28)$$

and the function  $g(t)$  becomes a constant.

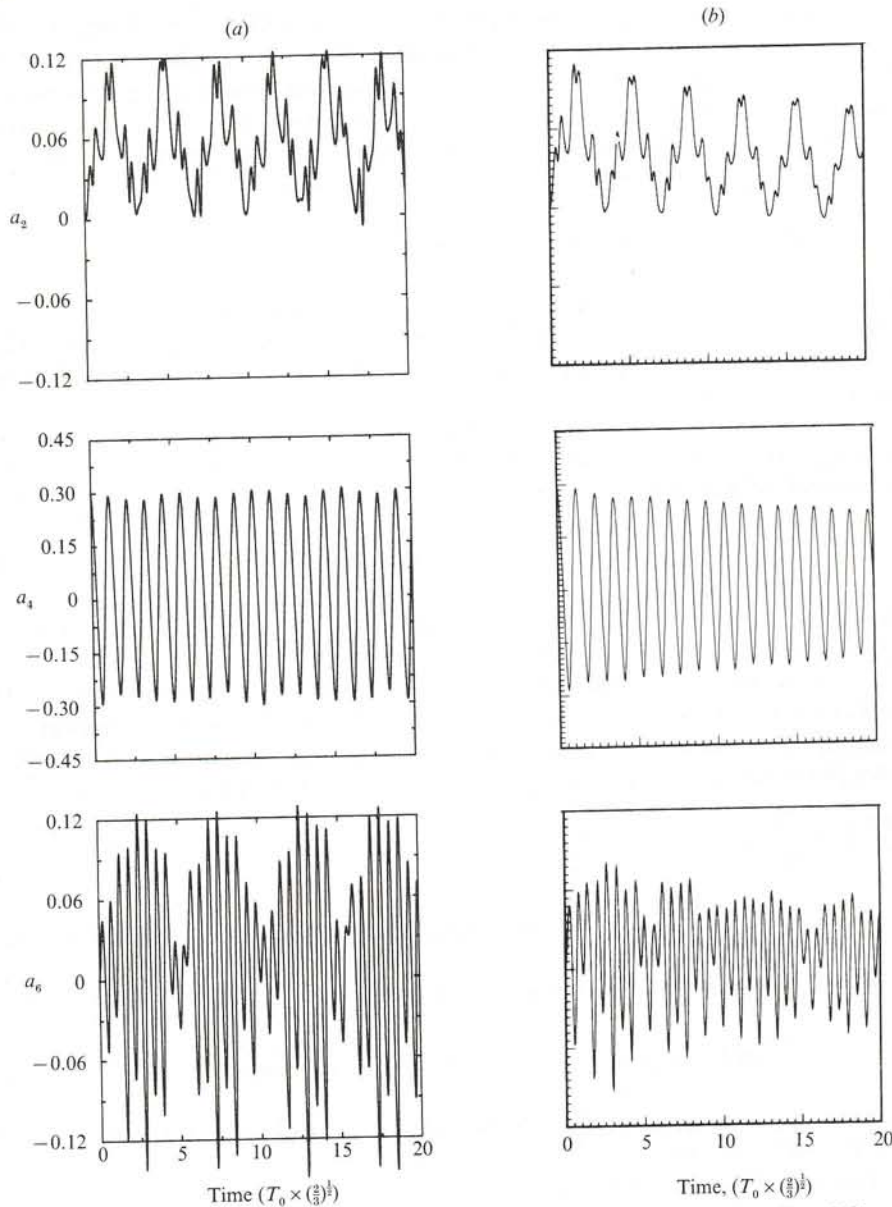


FIGURE 7. (a) The oscillation modes generated for initial conditions:  $a_4(t=0) = 0.3$ ,  $a_{2-6}(t=0) = \dot{a}_{2-6}(t=0) = 0$  using the present model, compared with (b) the corresponding calculations of Lundgren & Mansour (1988) (reproduced from their figures 7 and 8, pp. 501–502).

It should be pointed out that the proposed method, solving the dynamic boundary condition directly, is generally equivalent to the Hamilton principle (Sommerfeld 1978), which is usually used (Brosa *et al.* 1989; Natarajan & Brown 1987) to obtain a generalized differential equation of the droplet motion (like (27)). The problem is that the formal use of the Hamilton principle provides no information, like minimization error  $\mathcal{H}_{\text{rel}}^2$ , on the accuracy with which the assumed parameterization of the droplet surface fulfils the boundary condition for the pressure (14). For large oscillation amplitudes this is not guaranteed by the truncated expansion (5) and erroneous solutions can be obtained.

The final equations (21), (25), (27) are computed and solved numerically. The surface integrals resulting from (21) and (25) are calculated by the use of extrapolation in rational functions (Stoer 1972). The partial derivatives of the coefficients  $c_{li}$  with respect to the shape parameters  $a_i$  are obtained by polynomial extrapolation (Stoer 1972). Finally the ordinary differential equations (27) are integrated using a modified (by Fehlberg 1970) Runge-Kutta algorithm. The integration starts at  $t = 0$  with initial values of surface deformation parameters  $a_i$  and their velocities  $\dot{a}_i$ , subsequently calculating values for the following time steps. The accuracy per time step relative to the norm  $(a_2^2 + \dots + a_{l_{\max}}^2 + \dot{a}_2^2 + \dots + \dot{a}_{l_{\max}}^2)^{\frac{1}{2}}$  is better than  $10^{-3}$ .

A dimensionless form of the equations used in the computation is obtained with the help of the following scaling: [length] =  $R_0$ , [time] =  $T_0 = (R_0^3 \rho / 3\sigma)^{\frac{1}{2}}$  and [energy] =  $E_0 = (4\pi\sigma R_0^2)^{\frac{1}{2}}$ . To keep track of the overall accuracy, the total oscillation energy of the droplet (sum of kinematic and potential one) and all related minimization errors are monitored (see Appendix B). For a typical calculation with 300 time steps (two periods of the fundamental mode) the fluctuation of the total energy is below 1%. This calculation requires about 20 minutes CPU time on an IBM 3090-300E.

### 3.2. Comparison with other theoretical models

The reliability of the theoretical model was tested by comparing its results with the trajectories published by Lundgren & Mansour (1988), who calculated numerically the nonlinear oscillations of low-viscosity droplets. For this purpose we simulate the initial conditions given by these authors as an example in their paragraph 5.1 (p. 499), i.e.  $a_4(t=0) = 0.3$  and  $a_{2-6}(t=0) = \dot{a}_{2-6}(t=0) = 0$ . The comparison of the obtained trajectories for the first three even modes (uneven modes are not excited) is displayed in figure 7. The numerical analysis of Lundgren & Mansour, based on the boundary-integral method, describes a droplet surface with 101 points. This corresponds to the surface parameterization with a large number of modes. In spite of the fact that our description of the surface displacements is limited to 5 modes, and that the viscous effects are neglected in our calculations, it can be seen that the displayed oscillation trajectories are very similar to those reproduced from their paper. This confirms the adequacy of our model but also suggests that small viscosity effects incorporated in their model are mainly responsible for the amplitude decay and have a relatively small effect on the mode interactions.

Tsamopoulos & Brown (1983) and Dürr & Siekmann (1987) have studied, respectively analytically and numerically, non-viscous droplet oscillations. Both calculations confirm that nonlinearity of the fundamental mode is mainly characterized by a decrease of the oscillation frequency with increasing amplitude. In figure 8 data describing this dependence are recalculated from both papers and compared with those obtained from the present calculations and experiments. Although such a comparison has limits, it is worth noticing that all theoretical models predict a very similar dependence of the oscillation frequency on the amplitude, indicating their mutual consistency. The data evaluated from experiments (where the viscous damping was responsible for the decrease of the amplitude) are generally below the theoretical values.

### 3.3. Application to the experimental data

The presented calculations have been carried out for an inviscid liquid. Therefore, to compare quantitatively numerical results with experiment we must limit our attention to a single period of the fundamental mode, during which damping effects

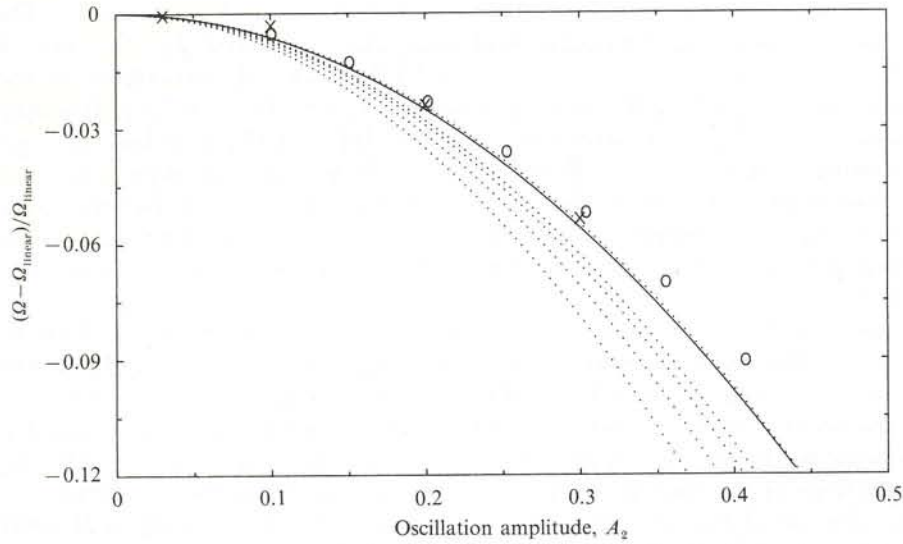


FIGURE 8. Relative frequency shift of the fundamental mode: typical values obtained in the present experiment (using the parameter  $\alpha_2$  in (7)) ( $\cdots$ ); values predicted by: Tsamopoulos & Brown (1983) (—), Dürr & Siekmann (1987) ( $\times$ ) and present theoretical model ( $\circ$ ).

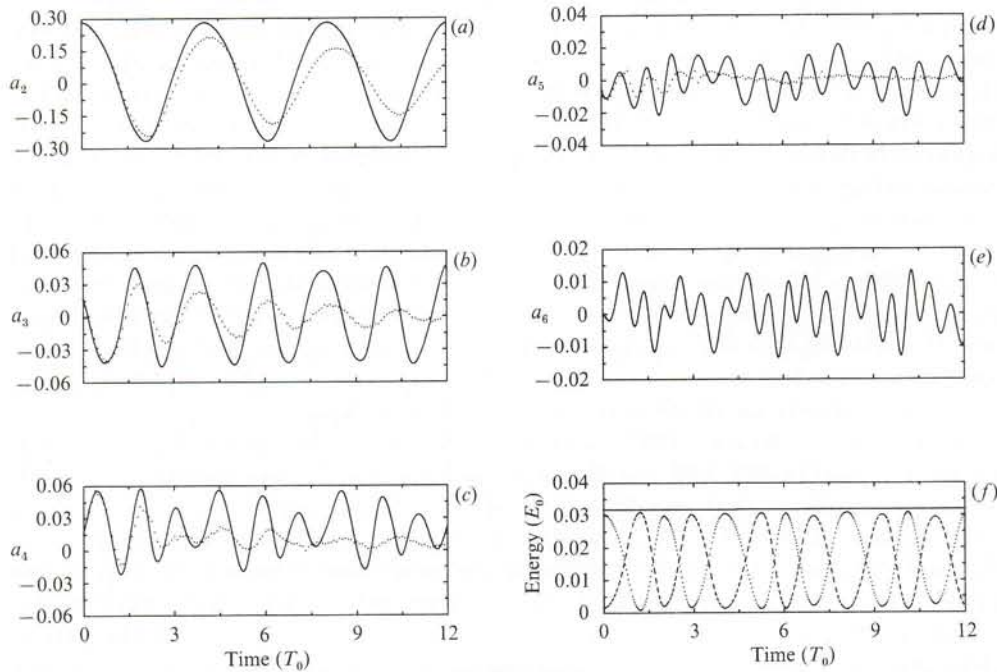


FIGURE 9(a-e). Theoretical simulation of oscillation amplitudes (—) compared with experimental data ( $\cdots$ ) from figure 3 for  $l = 2-6$ . (f) Calculated potential ( $\cdots$ ), kinetic (---) and total (—) energy of the droplet. The potential energy of the droplet in equilibrium is set to 0; time unit  $T_0$  is defined in the text.

are not too strongly manifested. However, to illustrate nonlinear effects better, we display in figure 9 several periods of the calculated and measured oscillations.

The numerical calculations in figure 9 are compared with the experimental results of figure 3. The calculation, performed for physical parameters characterizing the

droplet (radius, density and surface tension), begins at  $t_0 = 0.59$  ms, defined by the moment when the amplitude  $a_2$  reaches its first maximum. The initial values of  $a_{2-5}(t_0)$  and  $\dot{a}_{2-5}(t_0)$ , evaluated from experimental data, are (0.283, 0.017, 0.015, 0.006) and (0, -0.085, 0.109, -0.061) respectively, whereas  $a_6(t_0)$  and  $\dot{a}_6(t_0)$  are taken equal to zero. As we can see, during almost one period of oscillation the calculated trajectories of the deformation amplitude  $a_2(t)$  agree very well with experimental data. For longer time, owing to damping the discrepancies of the amplitudes begin to be evident. However, both the period of oscillation (or, more aptly, the location of amplitude extrema) and the general form of  $a_2(t)$  coincide very well with displayed experimental points. It is also worth noticing the similarities with the experimental data manifested by the higher surface modes  $a_3(t)$  and  $a_4(t)$ . For example  $a_3(t)$  shows a frequency modulation which appears simultaneously in the experimental and calculated curves. Furthermore, the nonlinear behaviour of  $a_4(t)$  is characterized by an amplitude modulation, which can be observed for both curves in figure 9(c). Similarly to the experimental observations, in the calculated oscillations the nonlinear effects become most evident for higher ( $l > 2$ ) modes.

To confirm the applicability of the theoretical model for the prediction of the surface tension of the liquid, the surface tension was calculated iteratively. The surface tension defines the characteristic time  $T_0$  needed for the calculation of the time derivatives of the initial velocities  $\dot{a}_{3-5}(t_0)$ . We start the calculation at the point where  $\dot{a}_2 = 0$  with an arbitrary value of surface tension. Then, the first period of the calculated oscillation trajectory  $a_2(t)$  is compared with the experimental data and a new value of the time unit  $T_0$ , hence of the surface tension, is used to calculate the velocities  $\dot{a}_{3-5}(t_0)$ . Repeating successively calculations until the period of  $a_2(t)$  does not change (three times was sufficient in our case), the final value of the surface tension is found. For the data of figure 3 the surface tension was found to be 22 mN/m, this is, remarkably, closer to the physical value than the asymptotic estimate of 19 mN/m, obtained for the same data using the linear approximation of equations (7) and (8).

#### 4. Conclusions

Both experimental and analytical results indicate that for amplitudes of the fundamental mode exceeding 10% of the droplet radius nonlinear effects cannot be neglected in the analysis of droplet oscillations. For short periods, the nonlinear effects observed in our experiments can be well predicted by the proposed inviscid theoretical model, confirming its applicability for prediction of the surface tension from large-amplitude oscillations of low-viscosity droplets.

This research was supported by the Deutsche Forschungsgemeinschaft (DFG). The authors wish to thank Priv. Doz. Dr U. Brosa for his suggestions and valuable discussions concerning the presented theoretical model.

#### Appendix A

The present study is limited to axially symmetric deformations of a droplet. The droplet is observed from one direction only, therefore the validity of the above assumption must be proved by monitoring the temporary deviation of the equilibrium radius  $R_0(t)$  of the droplet from its mean value  $\bar{R}_0$ . For this purpose

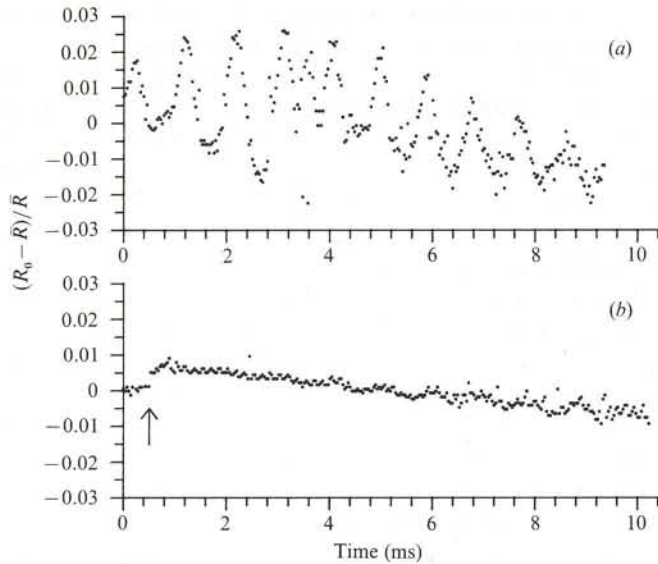


FIGURE 10. Temporal variation of the relative droplet radius. The arrow indicates the moment of merging with the satellite. (a) Typical effect of non-axially symmetric oscillations, (b) the droplet analysed in figure 10.

relative values of the radius  $(R_0 - \bar{R}_0)/\bar{R}_0$  are fitted to the linear function  $\mathcal{R}(t) = a \cdot t + b$ . Only such measurements, for which the standard deviation of the fit is below  $2 \times 10^{-3} \bar{R}_0$  are assumed to fulfil the assumption of axial symmetry and used for further analysis. To acquire the effect of monotonic radius variation on the oscillation frequency the empirical formula (7) includes the time variable normalization function:

$$N(t) = \left( \frac{\bar{R}_0}{\mathcal{R}(t)} \right)^{1/3}. \quad (\text{A } 1)$$

This modification, of minor significance in the present study, allows the analysis of oscillations of evaporating droplets, which will become one of our next aims.

Figure 10 displays two examples of time variation of the instantaneous relative value of a droplet radius evaluated from the experimental observations. The first example, figure 10(a), shows the typical effect of non-axially symmetric oscillations, not acceptable for our analysis; the second one, figure 10(b), displays the radius variation for the droplet analysed in figure 4.

## Appendix B

The numerical analysis of droplet oscillations we use is a least-squares approximation to the boundary conditions. The accuracy of this approximation depends on the truncation numbers  $l_{\max}$  and  $i_{\max}$  (equations (5) and (11)), and the maximal amplitude of the oscillations. To find the optimal truncation numbers control computations were done for the trajectories displayed in figures 3 and 9 by varying values of  $l_{\max}$  and  $i_{\max}$ . The initial values of  $a_i$  and  $\dot{a}_i$  are given in §3.3. The calculations are performed for the first period of the fundamental mode keeping the relative accuracy per time step below  $10^{-3}$ . Table 1 displays the time-average values

$l_{\max}$	$i_{\max}$	$\bar{E}/E_0$	$\max(\Delta E/\bar{E})$	$\max(\mathcal{H}_{\text{rel}}^2)$	$\max((\chi_{\text{rel}})_2^2)$	$\max((\chi_{\text{rel}})_3^2)$
3	7	$3.129 \times 10^{-2}$	$2.1 \times 10^{-2}$	$1.6 \times 10^{-2}$	$6.1 \times 10^{-3}$	$1.1 \times 10^{-2}$
4	8	$3.152 \times 10^{-2}$	$3.8 \times 10^{-3}$	$3.6 \times 10^{-3}$	$1.6 \times 10^{-3}$	$8.4 \times 10^{-3}$
5	10	$3.187 \times 10^{-2}$	$2.7 \times 10^{-3}$	$2.4 \times 10^{-3}$	$4.6 \times 10^{-4}$	$2.5 \times 10^{-3}$
5	11	$3.187 \times 10^{-2}$	$2.7 \times 10^{-3}$	$2.4 \times 10^{-3}$	$4.5 \times 10^{-4}$	$8.8 \times 10^{-4}$
6	12	$3.183 \times 10^{-2}$	$1.2 \times 10^{-3}$	$1.1 \times 10^{-3}$	$1.7 \times 10^{-4}$	$6.2 \times 10^{-4}$
7	13	$3.182 \times 10^{-2}$	$9.6 \times 10^{-4}$	$5.6 \times 10^{-4}$	$1.1 \times 10^{-4}$	$2.5 \times 10^{-4}$
8	14	$3.182 \times 10^{-2}$	$7.8 \times 10^{-4}$	$6.1 \times 10^{-4}$	$7.5 \times 10^{-5}$	$1.1 \times 10^{-4}$
9	14	$3.181 \times 10^{-2}$	$6.1 \times 10^{-4}$	$3.4 \times 10^{-4}$	$3.7 \times 10^{-5}$	$1.1 \times 10^{-4}$
10	14	$3.181 \times 10^{-2}$	$5.2 \times 10^{-4}$	$4.2 \times 10^{-4}$	$3.7 \times 10^{-5}$	$1.5 \times 10^{-4}$

$l_{\max}$	$i_{\max}$	$\max((\chi_{\text{rel}})_4^2)$	$\max((\chi_{\text{rel}})_5^2)$	CPU (min)
3	7	—	—	2
4	8	$1.5 \times 10^{-2}$	—	4
5	10	$4.6 \times 10^{-3}$	$2.3 \times 10^{-2}$	6
5	11	$4.6 \times 10^{-3}$	$7.8 \times 10^{-3}$	6.5
6	12	$1.2 \times 10^{-3}$	$6.1 \times 10^{-3}$	10
7	13	$1.2 \times 10^{-3}$	$2.1 \times 10^{-3}$	18
8	14	$4.3 \times 10^{-4}$	$1.3 \times 10^{-3}$	35
9	14	$2.9 \times 10^{-4}$	$1.3 \times 10^{-3}$	60
10	14	$3.1 \times 10^{-4}$	$1.7 \times 10^{-3}$	80

TABLE 1. Time averaged value of the total energy, its maximum relative deviation and maximum values of related minimization errors. The last column gives the required CPU-time.

of the total energy  $\bar{E}/E_0$  with their maximum relative deviation, and maximum values of the error functions  $\mathcal{H}_{\text{rel}}^2$  and  $\chi_{\text{rel}}^2$ . The approximate computation time is given in the last column of the table.

#### REFERENCES

- BROSA, U. 1988 Strongly dissipative modes. Unpublished paper, Universität Marburg.
- BROSA, U., GROSSMANN, S., MÜLLER, A. & BECKER, E. 1989 Nuclear scission. *Nucl. Phys. A* **502**, 423c–442c.
- CHANDRASEKHAR, S. 1959 The oscillations of a viscous liquid globe. *Proc. Lond. Math. Soc.* **9**, 141–149.
- CHANDRASEKHAR, S. 1961 *Hydrodynamic and Hydromagnetic Stability*, pp. 466–477. Clarendon.
- CHAUDHARY, K. C. & MAXWORTHY, T. 1980 The nonlinear capillary instability of a liquid jet. Part 3. Experiments on satellite drop formation and control. *J. Fluid Mech.* **96**, 287–297.
- DÜRR, H. M. & SIEKMANN, J. 1987 Numerical studies of fluid oscillation problems by boundary integral techniques. *Acta Astr.* **15**, 859–864.
- FEHLBERG, E. 1970 Klassische Runge–Kutta–Fromeln vierter und niedriger Ordnung mit Schrittweitenkontrolle und ihre Anwendung auf Wärmeleitungsprobleme. *Computing (Wien)* **6**, 61–71.
- HILLER, W. J. & KOWALEWSKI, T. A. 1989a Surface tension measurements by the oscillating droplet method. *Phys. Chem. Hydrodyn.* **11**, 103–112.
- HILLER, W. J. & KOWALEWSKI, T. A. 1989b Application of the frame transfer charge-coupled device for high speed imaging. *Opt. Engng* **28**, 197–200.
- HILLER, W. J., KOWALEWSKI, T. A. & STASICKI, B. 1989 High speed image recording. *Laser Optoelektronik* **21**, 64–68 (in German).
- LAMB, H. 1932 *Hydrodynamics*, 6th edn, pp. 473–475. Cambridge University Press.
- LUNDGREN, T. S. & MANSOUR, N. N. 1988 Oscillation of drops in zero gravity with weak viscous effects. *J. Fluid Mech.* **194**, 479–510.

- MILLER, C. A. & SCRIVEN, L. E. 1968 The oscillation of a fluid droplet immersed in another fluid. *J. Fluid Mech.* **32**, 417-435.
- NATARAJAN, R. & BROWN, R. A. 1987 Third-order resonance effect and the nonlinear stability of drop oscillation. *J. Fluid Mech.* **183**, 95-121.
- PROSPERETTI, A. 1977 Viscous effects on perturbed spherical flows. *Q. Appl. Maths* **35**, 339-352.
- PROSPERETTI, A. 1980a Normal-mode analysis for the oscillations of a viscous liquid drop immersed in another liquid. *J. Méc.* **19**, 149-182.
- PROSPERETTI, A. 1980b Free oscillations of drops and bubbles: the initial-value problem. *J. Fluid Mech.* **100**, 333-347.
- RAYLEIGH, LORD 1879 On the capillary phenomena of jets. *Proc. R. Soc. Lond.* **29**, 71-97.
- REID, W. H. 1960 The oscillations of a viscous liquid drop. *Q. Appl. Maths* **18**, 86-89.
- SOMMERFELD, A. 1978 *Theoretische Physik. Mechanik der deformierbaren Medien*, vol. III, §12. Thun-Frankfurt/M: Harri Deutsch.
- STASICKI, B., HILLER, W. J. & MEIER, G. E. A. 1990 A light pulse generator for high speed photography using semiconductor devices as a light source. *Opt. Engng* **29**, 821-827.
- STOER, J. 1972 *Einführung in die Numerische Mathematik I*, chap. 2. Springer.
- STRANI, M. & SABETTA, F. 1988 Viscous oscillations of a supported drop in an immiscible fluid. *J. Fluid Mech.* **189**, 397-421.
- TRINH, E. H., MARSTON, P. L. & ROBESY, J. L. 1987 Acoustic measurement of the surface tension of levitated drops. *J. Colloid Interface Sci.* **124**, 95-103.
- TRINH, E. & WANG, T. G. 1982 Large-amplitude free and driven drop-shape oscillations: experimental observations. *J. Fluid Mech.* **122**, 315-338.
- TSAMOPOULOS, J. A. & BROWN, R. A. 1983 Nonlinear oscillations of inviscid drops and bubbles. *J. Fluid Mech.* **127**, 519-537.
- VALENTINE, R. S., SATHER, N. F. & HEIDEGER, W. J. 1965 The motion of drops in various media. *Chem. Engng Sci.* **20**, 719-728.